SAND2018-13372J

Modelling Mechanical Behavior of an Additively Manufactured Metal Structure with Local Texture Variations: A Study on Model Form Error

Judith A. Brown[1,*], **Joseph E. Bishop**[1]

[1]Engineering Sciences Center, Sandia National Laboratories, Albuquerque, NM 87185

E-mail: `judbrow@sandia.gov, jebisho@sandia.gov`

* corresponding author

November 2018

Abstract. The repetitive rapid solidification that occurs in metal additive manufacturing (AM) processes creates microstructures distinctly different from wrought materials. Local variability in AM microstructures (either by design or unintentional) raises questions as to how AM structures should be modeled at the part-scale to minimize modeling error. The key goal of this work is to demonstrate *a posteriori* error estimation applied to an AM part. It is assumed that the actual microstructure is unknown and an approximate, spatially uniform material model is used. Error bounds are calculated for many reference models based on AM microstructures with elongated grain morphology and localized or global fiber textures during a post-processing step. The current findings promote confidence that *a posteriori* model form error estimation could be used effectively in mechanical performance simulations of AM parts to quickly obtain quantitative error metrics between an approximate model result and many microstructure-based reference models. The *a posteriori* error estimation introduces significant time savings compared to computing the full reference model solutions. Tight bounds on model form error are obtained when texture variations in the reference models occur on large length scales. For materials with property variation at small length scales, multi-scale error estimation techniques are needed to properly account for the many interfaces present between areas with different properties.

Keywords: additive manufacturing, error estimation, texture, mechanical properties
Submitted to: *Modelling Simul. Mater. Sci. Eng.*

1. Introduction

Recent advances in additive manufacturing (AM) technologies, in which parts are created from the layer by layer addition of material, are creating new possibilities in

Sandia National Laboratories is a multimission laboratory managed and operated by National Technology & Engineering Solutions of Sandia, LLC, a wholly owned subsidiary of Honeywell International Inc., for the U.S. Department of Energy's National Nuclear Security Administration under contract DE-NA0003525.

achievable part geometries and tailored material properties. Ultimately, mechanical performance is governed by the part's microstructural features and material properties, presence of defects, and residual stresses resulting from its complex thermal history [1]. In metal AM, the repetitive rapid solidification that occurs as each material layer is deposited creates unique microstructures with features distinctly different from traditionally processed materials. This aspect of AM renders the material properties throughout the part inseparable from the process parameters used to build it. As such, performance predictions and ultimately part qualification for metallic AM parts remains an active area of research [2, 3].

The microstructure within an AM part is highly dependent on the feedstock material, process parameters, part geometry, and geometric feature orientation with respect to the build direction. The evolving grain morphology and crystallographic orientation strongly depend on solidification dynamics in the melt pool and local temperature gradients [4, 5, 6, 7]. These in turn are affected by laser power [8], scan pattern [4, 6, 9, 10], scan velocity [11], part feature size and geometry [12, 13], and the number and spacing of parts on a build plate [5]. Various works in the literature identify microstructures that have strong fiber texture in the $\langle 1\,0\,0 \rangle$ crystal direction [14, 4, 15, 8, 12, 6, 9, 11, 16]. It has also been shown that certain scan patterns [4], dimensions of the part being built (small vs. bulk) [12], and different thermal gradients in different regions of a part [5, 13] can all result in texture variations within the part. This variability in local texture contributes to overall variability in mechanical performance. It has been shown by [17] that coupling of elongated grain morphology and texture can significantly affect mechanical behavior. While such variability may be undesirable, we also note that process-controlled microstructure to produce tailored local properties is a goal of AM efforts. Recent works have shown that local texture and grain morphologies can be modified by using different process parameters in different regions of a part [18, 19].

Variability in AM microstructures (either unintentional or by design) raises questions as to how AM structures should be modeled at the part-scale. Macroscopic material models used in part-scale simulations typically contain only a few internal state variables that represent the mean response of the material. Greater fidelity can be achieved from fine-scale models that account for various aspects of the microstructure, but these may be difficult to calibrate and/or prohibitively expensive to use in part-scale simulations. Additionally, the entire processing history of a part may not be known, and its microstructure may not be characterized. Thus, an approach where the primary simulation is conducted with a simple material model and supplemented with uncertainty quantification (UQ) or modeling error assessments becomes attractive. Uncertainty quantification of AM processes and parts is still new and largely focused on uncertainty in processing parameters [20, 21].

In this work, we draw from the body of literature on *a-posteriori* error-estimation techniques for solid mechanics [22, 23, 24] to quantify the error induced when using a simple, but approximate part-scale material model. In these methods, the errors resulting from use of an approximate material model in a mechanical performance simulation are assessed with respect to a more accurate, but presumably more complex, reference model during a post-processing step. Recent work by Brown and Bishop explored such methods applied to welds with textured microstructure [25]. A modelling approach in which an approximate material model can be used with adaptive material properties to minimize model form error has also been proposed [26]. The complexity of AM microstructures, however, requires special attention be paid to the reference model(s) used.

The goals of this work are to (1) develop a suite of reference models based on AM microstructures with local texture, and (2) demonstrate the application of *a posteriori* error estimation techniques to an AM part where it is assumed that the actual microstructure is uncertain. This paper is organized as follows. Section 2 presents a brief review of texture variations in AM parts and a discussion of scale separation. Section 3 presents a review of the theory for *a posteriori* model form error estimation. An example AM structure and finite element analysis details are given in Section 4. The approximate material model and the various microstructure-based reference models are introduced in Section 5. The resulting model predictions and error bounds are discussed in Section 6, and key conclusions are given in Section 7.

2. Texture variations and scale separation in metallic AM parts

In this section, we highlight several examples of AM parts with locally varying texture (Section 2.1). A brief discussion on scale separation for AM structures is also presented (Section 2.2). Many other features of the microstructure, such as cellular sub-grain structure, fine features at the melt pool overlap zones, compositional differences, and porosity can also affect the mechanical response. Incorporation of these mechanisms is beyond the scope of this paper and is not discussed here.

2.1. Texture variations in AM parts

In many AM builds, a microstructure with elongated columnar grains and a $\langle 1\,0\,0 \rangle$ fiber texture has been observed [8, 15, 12, 6, 9, 11, 16]. This texture typically occurs in cubic materials, where the $\langle 1\,0\,0 \rangle$ crystal direction is the preferred growth direction [27, 28]. Structural features of the part and the cyclic thermal history that occurs as the scan pattern is repeated during multi-layer builds also affects the microstructure. This can result in differently textured regions within a single AM part. Several examples are discussed here, to highlight that a uniform material property may not be representative of the material everywhere in the part.

For example, Thijs *et al* studied several different scan patterns and found repeated localized bands of elongated grains with $\langle 1\,0\,0 \rangle$ crystal orientations with spacing on the order of the melt pool widths even when a global texture was not present [4]. Niendorf *et al* [12] studied the effect of lattice strut dimensions on microstructures within a 316L stainless steel lattice structure manufactured by the Selective Laser Melting (SLM) process. Small-diameter lattice struts showed a highly anisotropic microstructure with strong ⟨1 0 0⟩ fiber texture, whereas larger struts processed under the same conditions showed a microstructure with little texture [12].

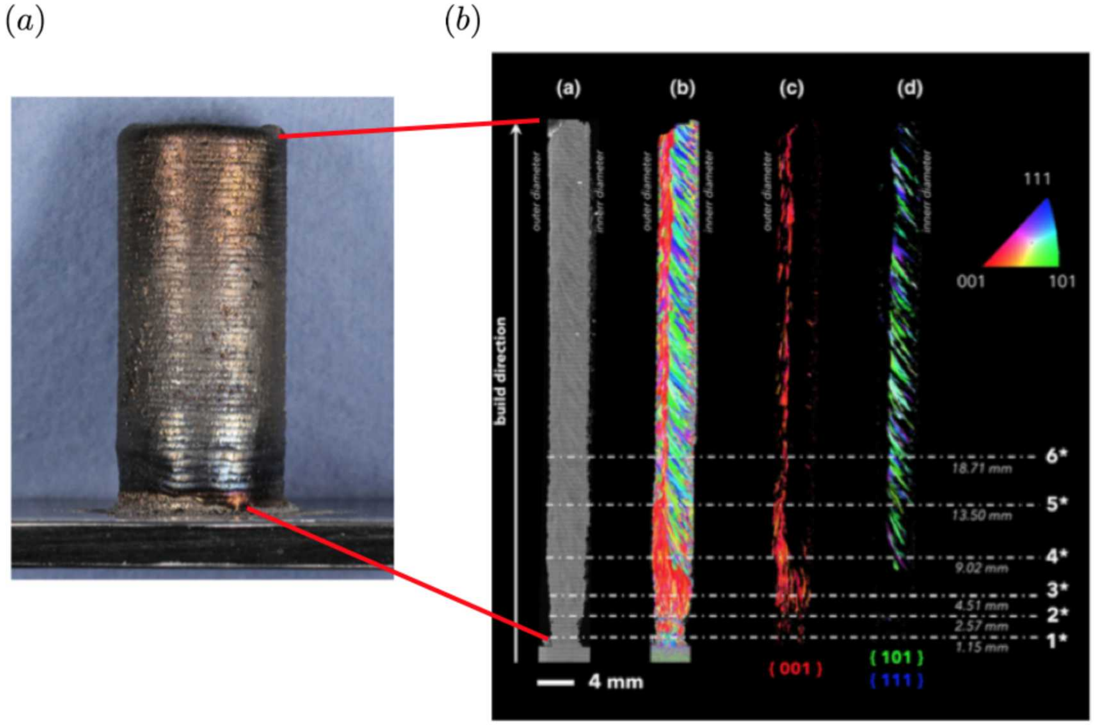

Figure 1. Additively manufactured 304L stainless steel tube. (a) side view of the as-built tube structure, (b) longitudinal EBSD scan along the height of the tube wall. (Adapted with permission from Springer Nature: Springer Nature, Comp. Mech., Johnson, Rodgers *et al* , 2017 ([13]).)

Johnson *et al* [13] recently studied a 304L stainless steel tube structure printed with a direct energy deposition (DED) process. Figure 1 shows the tube structure and EBSD scans along the entire length of the tube. The microstructure evolves from small equiaxed grains near the base into a transition region of nearly all ⟨1 0 0⟩ grains [13]. Further up the tube build, the interior of the tube shows mostly ⟨1 0 1⟩ and ⟨1 1 1⟩ grains with a concentric ring of ⟨1 0 0⟩ grains around the tube exterior wall [13].

A long-term goal of AM efforts is to achieve process-controlled local properties within an AM structure by producing different microstructures at specific locations. Notable works by Dehoff *et al* [19] and Popovich *et al* [18] demonstrate feasibility of this concept on a laboratory scale. Popovich *et al* recently manufactured functionally graded tensile bars from Inconel 718 and achieved sharp transitions between a fine-grained microstructure with no texture and a coarse-grained microstructure with strong ⟨1 0 0⟩ fiber texture by varying the laser power [18]. Corresponding transitions in elastic properties were also demonstrated [18].

2.2. Scale separation

The AM microstructures discussed in Section 2.1 present a challenge for mechancial performance modelling. Locally varying microstructure may violate the assumptions of scale separation, statistical homogeneity, and isotropy often used in part-scale simulations. The scale-separation approximation is crucial to macroscale solid-mechanics modeling since it provides a clear separation between the material and the response of the macroscale part modeled using continuum mechanics [29].

The actual length scales relevant to achieve scale separation are dependent on the particular part geometry and material microstructure. One heuristic definition is that the length scale of the macroscopic geometric features should be much larger than the average grain size. Additionally, if the part exhibits local regions with crystallographic texture that correspond to distinct mechanical properties (such as in [18]), then the length scale associated with changes in local texture must also be considered.

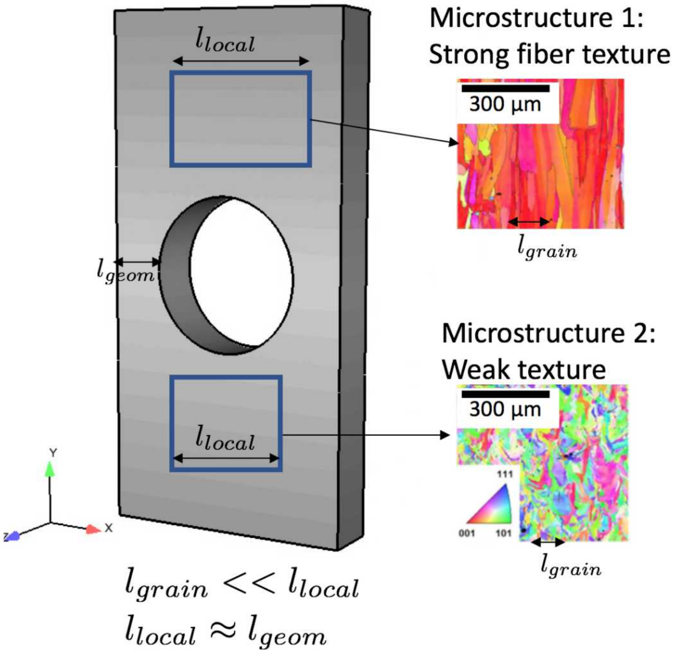

Figure 2. Schematic of variable microstructure regions in an AM structure. Regions with local texture may be on a comparable length scale to structural features. EBSD images adapted with permission from Springer Nature: Springer Nature, Met. Mat. Trans. B, Niendorf, Leuders, *et al* , 2013 ([8])

Figure 2 shows a schematic illustration of relevant length scales in an AM structure with local regions of distinctly different texture. These include the grain-scale (l_{grain}), length scale associated with an area of localized texture (l_{local}), and the part geometric features (l_{geom}). For cases where scale separation between the grain-scale and the structural features is violated, direct numerical simulation (DNS) of the microstructure can be used to model the grain-scale physics (for example, crystal plasticity). DNS provides arguably a more accurate representation of the material microstructure than macroscale models but can be prohibitively expensive when applied to engineering-scale structures. For example, DNS of a tube structure with embedded microstructure by Bishop *et al* [29] required approximately 30 million finite elements to resolve approximately 50,000 grains in the tube microstructure.

For engineering simulations, it is more likely that a single spatially uniform material property would be used to represent the entire structure. This modeling approach is computationally efficient, but assumes scale separation between the structural features and the length scale on which microstructure changes occur. This assumption may not be appropriate in many AM parts and could result in significant model form error for engineering quantities of interest.

3. Model Form error estimation

In this section, the theory of *a posteriori* error estimation is briefly reviewed and applied to an AM part. Section 3.1 gives a summary of the method used to bound errors arising from the use of an approximate material model with respect to a more accurate reference model [22, 23]. A discussion of the workflow that considers multiple reference models to represent the uncertainty of an unknown microstructure is given in Section 3.2. Ultimately, we are interested in multiscale model-form error estimation in engineering quantities of interest. However, this work focuses on single scale error assessments in the energy norm to highlight the unique challenges associated with developing reference models for AM structures. Additionally, we focus here on linear elasticity as a first step towards the more general nonlinear case.

3.1. Error Estimation Theory

Consider the general boundary value problem of a body B with surface Γ subjected to the boundary conditions of applied surface tractions and/or surface displacements. For conditions of static equilibrium and the absence of body forces, the motion of this body is governed by

$$\nabla \cdot \boldsymbol{\sigma} = \mathbf{o} \tag{1}$$

with boundary conditions $\boldsymbol{u} = \bar{\boldsymbol{u}}$ on Γ_u and $\boldsymbol{\sigma} \cdot \boldsymbol{n} = \boldsymbol{t}$ on Γ_t. Here $\boldsymbol{\sigma}$ is the Cauchy stress, $\boldsymbol{u}$ is the displacement field inside the body, $\bar{\boldsymbol{u}}$ is the applied displacement, $\boldsymbol{n}$ is the surface normal, and $\boldsymbol{t}$ is the applied traction. The displacement field $\boldsymbol{u}$ is obtained via the solution of (1) together with the equations of strain-displacement compatibility and the material constitutive law relating stress to strain.

For linear elastic materials, the relationship between stress and strain is given by

$$\boldsymbol{\sigma} = \mathbb{C}\boldsymbol{\epsilon}, \tag{2}$$

where $\boldsymbol{\sigma}$ is the stress tensor, $\mathbb{C}$ is the fourth-order elasticity tensor, and $\boldsymbol{\epsilon}$ is the linear strain tensor. The compliance tensor $\mathbb{S}$ is defined as the inverse of $\mathbb{C}$, so that $\mathbb{S} = \mathbb{C}^{-1}$. The general form of $\mathbb{C}$ can be fully anisotropic and spatially varying throughout the body as $\mathbb{C}(\boldsymbol{x})$. We let this general form of $\mathbb{C}$ be the reference material model, and assume that it is the closest representation of the AM structure's local elastic properties. We also introduce an approximate material model with an approximate elasticity tensor, $\mathbb{C}^0$, which contains known simplifications from $\mathbb{C}$. For the present example, we restrict $\mathbb{C}^0$ to be isotropic and spatially uniform.

We assume that it is difficult to use the reference material model in part-scale finite element simulations due to constraints such as computational expense. Instead, the simulation is performed using the approximate material model to obtain an approximate displacement solution $\boldsymbol{u}^{0,h}$, where h denotes a measure of mesh size. The associated stress and strain fields obtained from this approximate solution are $\boldsymbol{\epsilon}^0$ and $\boldsymbol{\sigma}^0$ respectively. While computational expense may be small for the linear elastic models studied here, the general methodology demonstrated through this example could be extended to much more complex models where expense is a limiting factor.

The error $\boldsymbol{e}$ between the approximate displacement field and the true displacement field $\boldsymbol{u}$ that would be obtained with the reference model is defined as

$$\boldsymbol{e} \doteq \boldsymbol{u} - \boldsymbol{u}^{0,h}. \tag{3}$$

For the following analysis, the energy norm of the displacement field for a domain Ω is defined as

$$||\boldsymbol{u}(x)||_E \doteq \left(\int_\Omega \boldsymbol{\epsilon}(x) : \mathbb{C}(x)\boldsymbol{\epsilon}(x) d\Omega \right)^{1/2}. \tag{4}$$

Using the triangle inequality property of norms, the error may be bounded in the energy norm as

$$||\boldsymbol{e}||_E \leq ||\boldsymbol{u} - \boldsymbol{u}^0||_E + ||\boldsymbol{u}^0 - \boldsymbol{u}^{0,h}||_E. \tag{5}$$

The first term $||\boldsymbol{u} - \boldsymbol{u}^0||_E$ is the norm of error due to material model form. The second term $||\boldsymbol{u}^0 - \boldsymbol{u}^{0,h}||_E$ is the norm of the error due to discretization methods used to obtain the solution. Here we assume that the discretization error is much smaller than the model form error such that discretization error may be ignored.

Zohdi *et al* [22] obtained the following upper bound on the energy norm of the model form error

$$||\boldsymbol{u} - \boldsymbol{u}^0||_E^2 = \int_\Omega (\boldsymbol{\epsilon}^0 - \boldsymbol{\epsilon}) : \mathbb{C}(\boldsymbol{\epsilon}^0 - \boldsymbol{\epsilon}) d\Omega \leq \int_\Omega (\boldsymbol{\epsilon}^0 - \bar{\boldsymbol{\epsilon}}) : (\bar{\boldsymbol{\sigma}} - \boldsymbol{\sigma}^0) d\Omega \tag{6}$$

where $\bar{\boldsymbol{\epsilon}}$ and $\bar{\boldsymbol{\sigma}}$ are calculated from the approximate stress or strain fields and the reference material properties as $\bar{\boldsymbol{\sigma}} \doteq \mathbb{C}\boldsymbol{\epsilon}^0$ and $\bar{\boldsymbol{\epsilon}} \doteq \mathbb{S}\boldsymbol{\sigma}^0$. The bound on the right hand side of (6) is obtained entirely from known quantities and is calculated as a post-processing step once the approximate solution is obtained. The total bound on the right hand side of (6) is represented as the quantity Z^2, so that

$$Z^2 \doteq \int_\Omega (\boldsymbol{\epsilon}^0 - \mathbb{S}\boldsymbol{\sigma}^0) : (\mathbb{C}\boldsymbol{\epsilon}^0 - \boldsymbol{\sigma}^0) d\Omega. \tag{7}$$

The integrand of (7) is a local error indicator, defined as

$$\zeta^2 \doteq (\boldsymbol{\epsilon}^0 - \mathbb{S}\boldsymbol{\sigma}^0) : (\mathbb{C}\boldsymbol{\epsilon}^0 - \boldsymbol{\sigma}^0). \tag{8}$$

The local error indicator ζ^2 can be written in a strain form or a stress form (see for example, Bishop and Brown [26]). Here, we use the strain form, written as

$$\zeta^2 \doteq (\boldsymbol{\epsilon}^0 - \mathbb{S}(\mathbb{C}^0\boldsymbol{\epsilon}^0)) : (\mathbb{C}\boldsymbol{\epsilon}^0 - (\mathbb{C}^0\boldsymbol{\epsilon}^0)). \tag{9}$$

Note that the local error indicator, ζ^2, is not a strict bound on the true local error. It only identifies errors due to local differences in the approximate material properties, $\mathbb{C}^0$, and the reference material properties, $\mathbb{C}$. It cannot account for pollution errors introduced from non-local effects in other regions of the structure [30]. For example, if $\mathbb{C}^0 = \mathbb{C}$ locally, the value of ζ^2 would be zero while the true error may be non-zero due to pollution errors introduced from other regions where $\mathbb{C}^0 \neq \mathbb{C}$. However, the total error bound Z^2 remains a strict bound for the energy norm of error in the entire part.

In the case of finite element analysis, the total bound Z^2 can be written as the sum of local contributions from each element as

$$Z^2 = \sum_{M=1}^{N} \left(\zeta_M^2 V_M\right), \tag{10}$$

where ζ_M^2 and V_M are the local error indicator and volume of each finite element, respectively, and N is the total number of elements.

3.2. Workflow with multiple reference models

For AM structures, the exact microstructure may be unknown and could possibly be variable throughout different regions of the structure. In such cases, choosing a single, deterministic, reference model is challenging and may require complex process-structure-property simulations to ensure that the reference model truly represents the AM material. This could be time consuming and expensive. As an alternate approach, we develop a suite of multiple reference models based on idealized versions of *possible* microstructures, and use these to generate a range of error bounds. This provides a way to assess the accuracy of predictions made by the approximate model that incorporates the epistemic uncertainty introduced by not knowing the true microstructure. With careful design of the reference models, the error bound with respect to the true microstructure is assumed to be within the range of bounds generated.

A schematic of this workflow is shown in Figure 3. The primary simulation is performed once with the approximate material model. A range of error bounds is then generated with respect to multiple reference models *a posteriori* to the main simulation with a special post-processing code. This moves assessment of material variability and uncertainty to the postprocessing step, which is much less computationally expensive than conducting a forward simulation with each reference model.

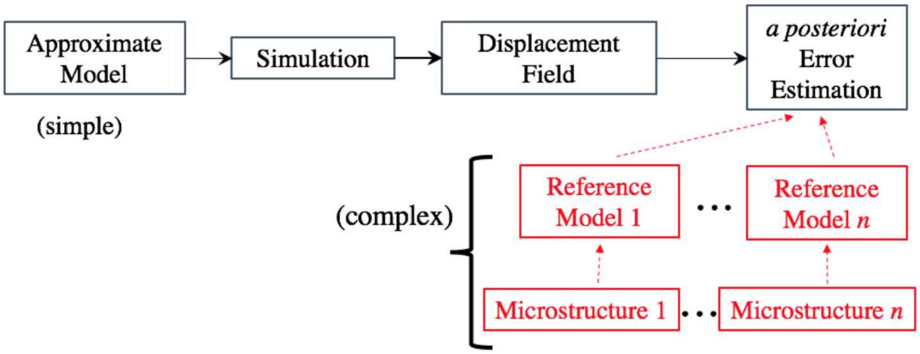

Figure 3. Workflow for *a posteriori* error estimation with many microstructurally based reference models.

4. Example AM part and boundary value problem

For an example of the error estimation workflow, we consider an AM plate with a center hole loaded in uniaxial tension. The geometry and plate dimensions are shown in Figure 4a. The build direction, scan direction, and the structural coordinate system X, Y, Z are indicated. The plate is composed of 20 individual layers 0.5 mm high with a total height of 10mm. This layer thickness of 0.5 mm is typical of the upper range seen in direct energy deposition processes [5].

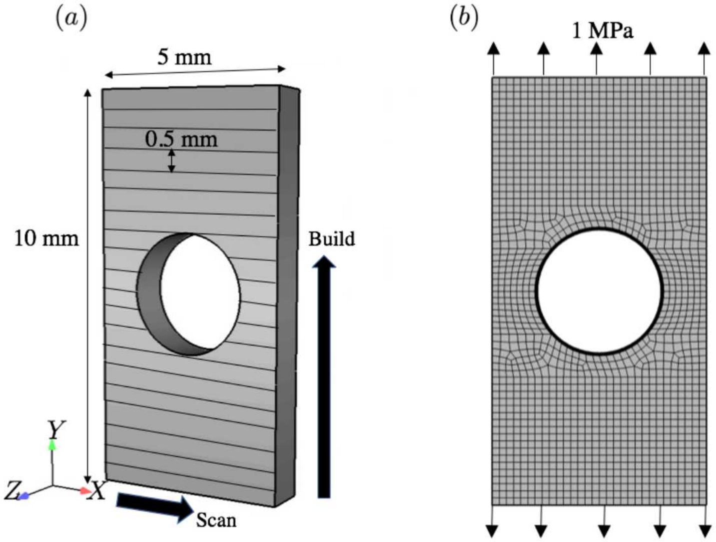

Figure 4. Plate structure with center hole. (a) Plate geometry and dimensions with layer thickness shown. The AM build and scan directions are indicated. (b) Coarse finite element mesh (9,342 elements) and applied traction boundary condition. Simulations were performed on this mesh with one level of hierarchical refinement (74,736 elements).

Table 1. Homogenized elastic properties used for the material models: Young's modulus, E, Poisson's ratio, ν, and Shear Modulus, G. Values of Young's moduli and shear moduli, G, are given in GPa.

	E_{11}	E_{22}	E_{33}	ν_{23}	ν_{13}	ν_{12}	G_{23}	G_{13}	G_{12}
Isotropic	200	200	200	0.3	0.3	0.3	75	75	75
Pure Fiber Texture	143	143	91.8	0.610	0.610	0.115	126	126	64

The applied traction boundary conditions and finite element mesh are shown in Figure 4b. The meshing software Cubit [31] was used to create both the geometry and mesh of the plate. The plate was first meshed with 9,342 hexahedral elements to produce the mesh shown in Figure 4b. The simulations were performed on a mesh with one level of hierarchical refinement (74,736 elements). Unit normal tractions of 1 MPa were applied to the upper and lower surfaces of the plate (Figure 4b) to explore the small-strain behavior. The finite element simulations were performed using the Sierra/SM finite element software [32].

5. Approximate and reference material models

We introduce the approximate material model and the suite of reference models developed as idealized versions of possible AM microstructures. The material considered here is AISI 304L stainless steel. This material is expected to have a primarily austenitic microstructure (γ-Fe) in AM structures, similar to AM 316 stainless steels [5, 16]. The austenite crystal structure is face-centered cubic (FCC) and has three independent elastic constants: $C_{11} = 205$ GPa, $C_{12} = 138$ GPa, and $C_{44} = 126$ GPa [33]. The anisotropy ratio $A \doteq 2C_{44}/(C_{11} - C_{12}) = 3.8$ for this crystal. For an isotropic crystal, $A = 1$. The relatively large anisotropy ratio for austenite suggests that the homogenized material properties of highly textured microstructures will be anisotropic [34].

5.1. Approximate material model

For the approximate material model, we assume that the material properties are spatially uniform throughout the structure. We use isotropic elasticity with nominal values for stainless steel of Young's modulus $E = 200$ GPa and Poisson's ratio $\nu = 0.3$. This approach is attractive for its simplicity, but may not be representative of textured AM microstructures and would not account for microstructure variations.

5.2. Reference material models

The set of reference models is based on the highly textured microstructures with elongated grains seen in many AM structures (see Section 2). A pure $\langle 1\,0\,0 \rangle$ fiber texture is used to represent the limiting case when a strong texture is present. The structure is modeled entirely at the macroscale with homogenized material properties.

This approach assumes that scale separation is valid between the individual grain length scale and the length scale associated with localized texture variations. In this case, homogenized properties can then be used to represent a local region with distinct $\langle 1\,0\,0\rangle$ fiber texutre. Scale separation is not implied, however, between the macroscale geometric features and individual regions with local texture. As such, we allow the orientation of the homogenized material properties to vary spatially throughout the part, such that localized regions with different properties can be resolved.

5.2.1. Homogenized properties of pure fiber texture We use a representative volume element (RVE) approach to obtain homogenized elastic properties of 304L stainless steel with a pure $\langle 1\,0\,0\rangle$ fiber texture.

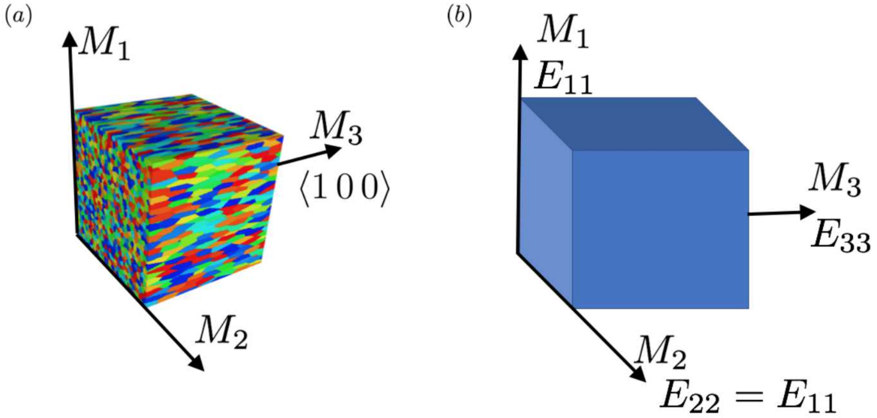

Figure 5. (a) The representative volume element (RVE) used to obtain homogenized material properties for the reference material model. Colors represent unique grains. (b) Material point with homogenized macroscale properties and material directions.

A material coordinate system, M_1, M_2, and M_3 represents the homogenized material's principal directions. Each grain's crystallographic orientation is aligned such that the $\langle 1\,0\,0\rangle$ direction coincides with the material direction M_3. The crystal orientations in the M_1 - M_2 plane are uniformly random, such that a pure $\langle 1\,0\,0\rangle$ fiber texture is obtained. Grain morphologies in the M_1 - M_2 plane were generated by classical Voronoi tessellation techniques, such that each Voronoi cell is used to represent a unique grain. The grains were then elongated in the M_3 direction by a ratio of 4:1 to approximate the elongated grain structure that can be present in AM materials. The RVE and associated effective material directions, M_1, M_2, and M_3 are shown in Figure 5 with color representing unique grains.

The macroscale effective elastic constants are obtained from computational homogenization of the RVE [35]. Further details on the RVE generation and homogenization process are available in [26]. The resulting homogenized material is transversely isotropic and has 5 independent elastic constants that are oriented with respect to the material coordinate system. Elastic constants for both the isotropic and pure fiber textured material are given in Table 1.

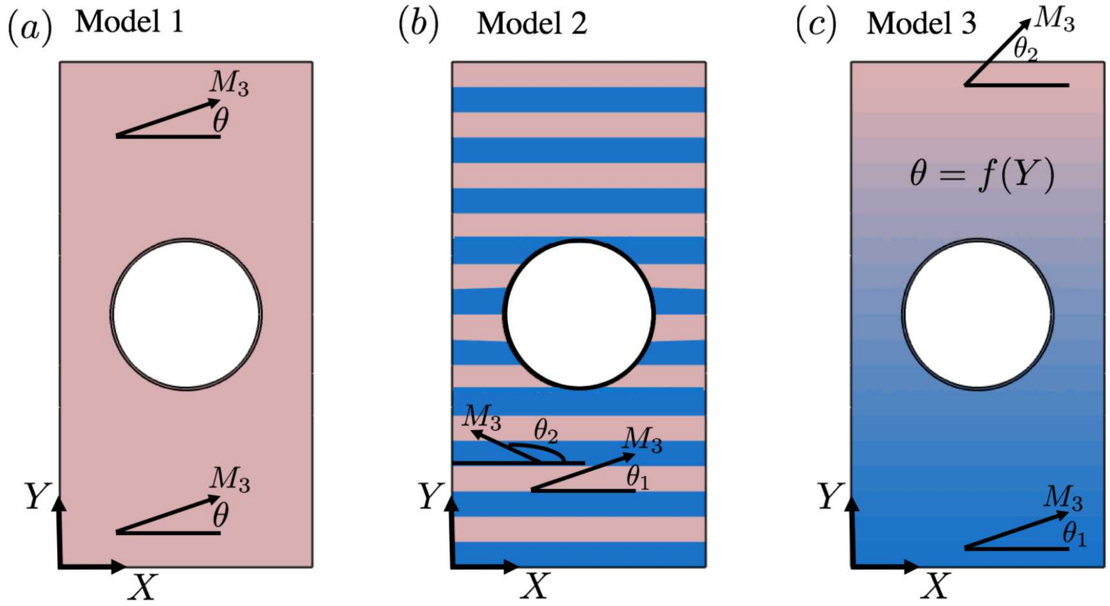

Figure 6. Reference models with spatially varying material orientation. (a) Model 1 with constant material orientation, (b) Model 2 with material orientation that alternates per layer, (c) Model 3 with material orientation that linearly varies as a function of Y.

5.2.2. Spatially varying material orientations Using standard coordinate transformation techniques for tensors, the homogenized transversely isotropic properties and material coordinate system are transformed to the global coordinate system for each reference model. Figure 6 shows the three different spatial distributions of properties considered. These are designed to be idealized versions of several microstructures reported in the literature. The angles θ, θ_1, and θ_2 represent the angle between the material M_3 direction, in which the $\langle 1\,0\,0\rangle$ grains are oriented, and the global X direction which corresponds to the scanning direction. We designate these as Models 1-3 to differentiate between each case in the following discussion.

Model 1 (Figure 6a) is an idealization that the as-deposited AM material develops a fiber texture that stays oriented at a constant angle θ with respect to the scanning plane throughout the entire structure. This is based on microstructures produced by long vector unidirectional scan patterns and high laser powers, such as in [8]. Model 2 (Figure 6b) is idealized such that the fiber texture alternates direction between angles θ_1 and θ_2 with each successive layer. This type of microstructure has been observed with bi-directional, long vector scan strategies, as in [6]. Model 3 (Figure 6c) has a linearly varying orientation gradient from angle θ_1 at the bottom of the structure to angle θ_2 at the top of the structure. This type of orientation gradient has been correlated with different scan velocities [11] and changing build surface normals with respect to the laser incidence angle [14].

6. Results and discussion

As a case study, we present error estimation results considering the reference Models 1-3 with fixed material orientation angles. We then present ranges of error bounds obtained from these reference models with multiple combinations of material orientations.

6.1. Case study with fixed material orientation angles

The material orientation angles for the three reference models were chosen based on additively manufactured structures reported in the literature. For Model 1, $\theta = 60°$ as has been reported for long vector, unidirectional scans [6, 9]. For Model 2, $\theta_1 = 45°$ and $\theta_2 = 90°$ which is idealized from microstructures reported for 316 stainless steel manufactured by DED processes [5]. The Model 3 structure has material orientation that linearly varies between $\theta_1 = 0°$ at the bottom and $\theta_2 = 90°$ at the top. This is explored as a limiting case where the material orientation shifts from being parallel to the scan direction in the initial few layers to being parallel to the build direction near the top of the build.

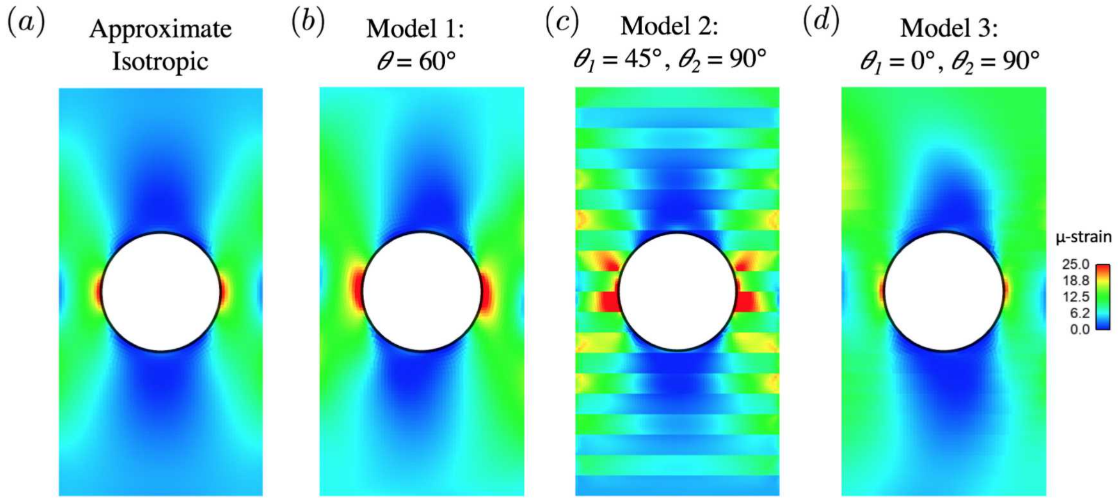

Figure 7. Results from finite element simulations showing axial strain fields (ϵ_{yy}) for: (a) approximate model (isotropic, uniform properties), (b) Model 1 with $\theta = 60°$, (c) Model 2 with $\theta_1 = 45°$ and $\theta_2 = 90°$, and (d) Model 3 with $\theta_1 = 0°$ and $\theta_2 = 90°$

6.1.1. Stress and strain response The axial strain fields (ϵ_{yy}) and the von Mises stress fields for each model are shown in Figure 7 and Figure 8, respectively. For the approximate model (Figures 7a, 8a), both fields are smooth and symmetric about the hole as expected for a structure consisting of a spatially uniform, isotropic material.

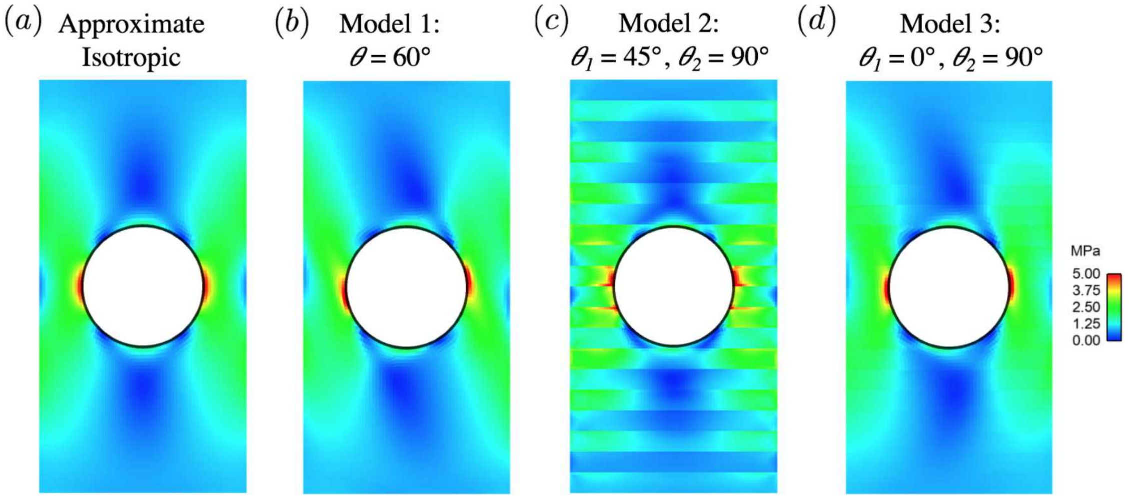

Figure 8. Results from finite element simulations showing von Mises stress fields for: (a) approximate model (isotropic, uniform properties), (b) Model 1 with $\theta = 60°$, (c) Model 2 with $\theta_1 = 45°$ and $\theta_2 = 90°$, and (d) Model 3 with $\theta_1 = 0°$ and $\theta_2 = 90°$

The hole acts as a stress concentrator, with the largest stresses and strains occurring at the left and right edges of its mid-plane.

The fully computed response of the three reference structure models is also presented for comparison to the approximate model response. For Model 1 (Figures 7b, 8b), the maximum strain occurs at the left and right edges of the hole, but the area with higher stresses and strains is rotated with respect to the structure centerlines. This results as the material axes in Model 1 are not aligned with the loading axis. Since the structure for Model 1 has a spatially uniform material orientation, the fields remain smooth without noticeable discontinuities at layer interfaces.

The response of Model 2 (Figures 7c, 8c) shows significant effects of the alternating material orientations for each layer. The highest strain and stress are at the mid-plane of the hole, but sharp discontinuities in both stress and strain are evident at the interfaces between each layer. Different behavior is seen in the $\theta_1 = 45°$ and $\theta_2 = 90°$ layers. The $\theta_1 = 45°$ layers have the material M_3 axis aligned at 45° with respect to the applied load along the structural Y axis. The $\theta_2 = 90°$ layers have the M_3 axis aligned directly parallel to the applied load. Since the material M_3 direction has a Young's modulus value E_{33} that is much lower than the other two material directions, it follows that layers with the $\theta_2 = 90°$ material orientation have higher strains compared with the layers that have the $\theta_1 = 45°$ material orientation. Such layer interfaces with sharp change in properties have been produced by AM processes, as demonstrated by Popovich *et al* [18] who produced functionally graded Inconel 718 by AM that exhibited distinct regions with different textures. Mechanical testing of this material showed a 50% reduction in Young's modulus for strong fiber textured $\langle 1\,0\,0 \rangle$ regions oriented with the load axis compared to fine grained equiaxed regions, and DIC revealed sharp gradients in strain at the region interfaces [18]. Hitzler *et al* [36] have also shown that Young's modulus of

AM parts can vary significantly depending on the orientation of the building direction with respect to the loading direction.

The response of Model 3 (Figures 7d, 8d) also exhibits effects of the local material orientation of each layer changing with respect to the applied load direction. In this case, the entire region of the plate above the hole has larger strain compared to the other models. This is due to the upper layers of the plate having material M_3 orientations that are approaching 90°, which aligns the least stiff material direction with the applied load. The layer interfaces are seen faintly here, but show a much less pronounced effect than Model 2. This is because the material orientation angle changes between any two layers are much more gradual in Model 3.

These results show that structural features tend to govern the global part response, while material variations generally contribute more to the local response. Similar observations were made by Bishop *et al* [29, 34] who compared direct numerical simulation (DNS) of parts including embedded microstructure with the macroscale solution using homogenized material properties. In these works, the mean stress and strain fields obtained by DNS were reasonably similar to the homogenized macroscale solution, but large fluctuations in the local stress and strain fields were also present due to the embedded microstructure [29, 34]. Such local variations would be particularly important to capture when predicting fatigue and fracture initiation. The current study of several idealized AM microstructures shows that if the material variations occur on a length scale that is small compared to the structure (Model 2), the effect may be local stress magnification or introduction of large local strain gradients. If the material variation occurs across a large length scale, (Model 3), the entire structure response may be altered. These impacts of material variability are especially relevant for AM parts and reinforce the need for computationally efficient ways to evaluate different microstructure-based models to supplement part performance analysis.

6.1.2. Error Estimation Figure 9 shows the local error indicator contours, ζ^2, for reference Models 1-3 with fixed orientation angles. The error indicators in Figure 9 are computed during the post processing step (see (8)), and do not require finite element computations with the reference models. To verify that these local error indicators provide accurate spatial representation of the true error, the local exact error between the finite element solutions of each reference model and the approximate model is shown in Figure 10. We define the local exact error, ω^2, as the quantity inside the integrand on the lefthand side of (6):

$$\omega^2 = \int_\Omega (\boldsymbol{\epsilon}^0 - \boldsymbol{\epsilon}) : \mathbb{C}(\boldsymbol{\epsilon}^0 - \boldsymbol{\epsilon}) d\Omega \tag{11}$$

Comparing the local exact errors in Figure 10 with the local error indicators in Figure 9, the spatial distributions are qualitatively very similar. Additionally, regions with high local error indicator (Figure 9) correspond to regions that show the most differences in the stress and strain fields between the approximate model and the reference models (Figures 7 - 8). The effect of layers with alternating material

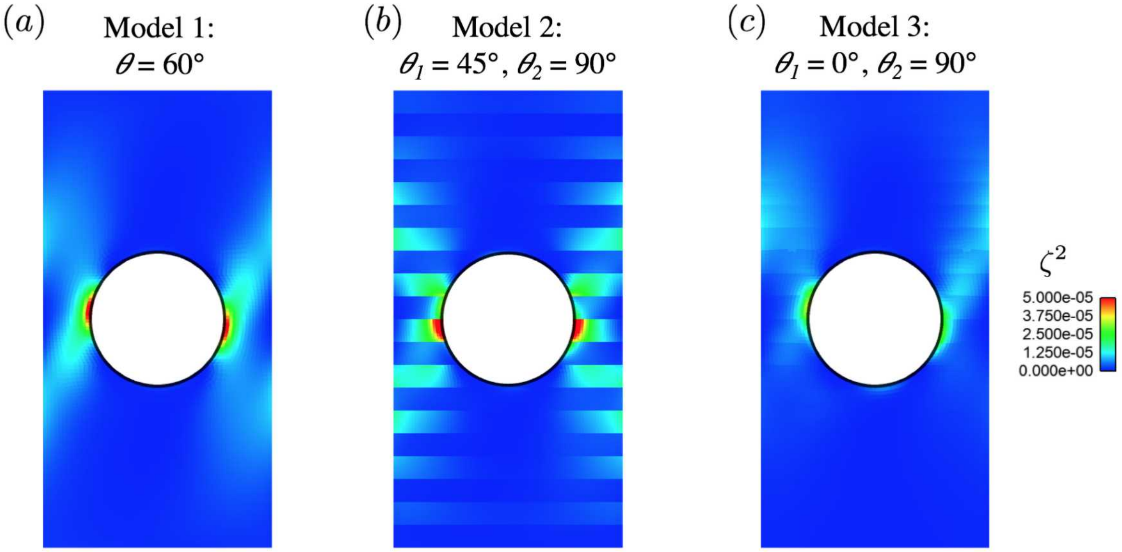

Figure 9. Contours of local error indicator ζ^2 between the isotropic approximate model and each reference model: (a) Model 1 with $\theta = 60°$, (b) Model 2 with $\theta_1 = 45°$ and $\theta_2 = 90°$, and (c) Model 3 with $\theta_1 = 0°$ and $\theta_2 = 90°$.

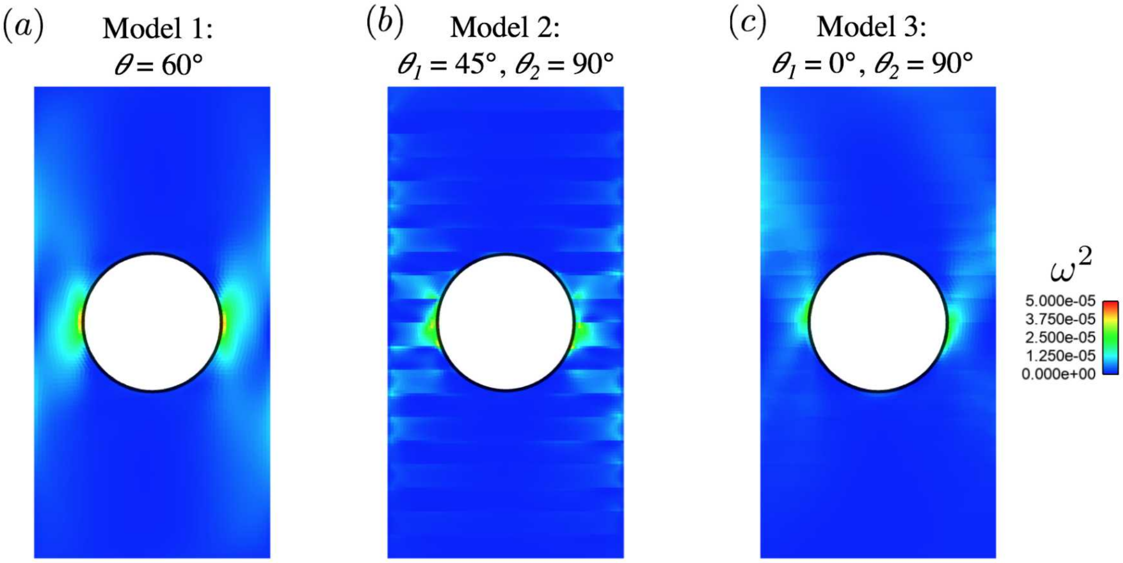

Figure 10. Local exact error ω^2 between the isotropic approximate model and each reference model: (a) Model 1 with $\theta = 60°$, (b) Model 2 with $\theta_1 = 45°$ and $\theta_2 = 90°$, and (c) Model 3 with $\theta_1 = 0°$ and $\theta_2 = 90°$.

orientations is clearly seen in Figure9b. The error indicator is higher in the layers oriented with $\theta_2 = 90°$ and exhibits sharp discontinuities at the layer interfaces. In Figure 9c, the local error indicator has the highest values in the top half of the structure due to the gradient of reference material orientation along the Y direction. This shows that the error indicators, which are calculated *a posteriori*, provide a good indication

Table 2. Comparison of the error bound, Z, and exact error computed between the approximate model and each reference model.

	θ_1	θ_2	Layer Orientation	$\frac{Z}{\lvert\lvert \boldsymbol{u}^0 \rvert\rvert_E}$	$\frac{\lvert\lvert \boldsymbol{u}^0 - \boldsymbol{u} \rvert\rvert_E}{\lvert\lvert \boldsymbol{u}^0 \rvert\rvert_E}$	$\eta \doteq \frac{Z}{\lvert\lvert \boldsymbol{u}^0 - \boldsymbol{u} \rvert\rvert_E}$
Model 1	60	–	Constant	0.6255	0.6095	1.0263
Model 2	45	90	Alternating	0.6591	0.5239	1.2579
Model 3	0	90	Gradient $f(Y)$	0.5449	0.5307	1.0268

Table 3. Exact errors in quantities of interest (strain energy, stress, strain, stretch) between the approximate model and each reference model.

	θ_1	θ_2	Layer Orientation	$\frac{\lvert W^0 - W \rvert}{W^0}$	$\frac{\lvert\lvert \boldsymbol{\sigma}^0 - \boldsymbol{\sigma} \rvert\rvert}{\lvert\lvert \boldsymbol{\sigma}^0 \rvert\rvert}$	$\frac{\lvert\lvert \boldsymbol{\epsilon}^0 - \boldsymbol{\epsilon} \rvert\rvert}{\lvert\lvert \boldsymbol{\epsilon}^0 \rvert\rvert}$	$\frac{\lvert \Delta(\boldsymbol{u_2})^0 - \Delta \boldsymbol{u_2} \rvert}{\Delta(\boldsymbol{u_2})^0}$
Model 1	60	–	Constant	0.3017	0.1187	0.8555	0.3028
Model 2	45	90	Alternating	0.3480	0.4057	0.7098	0.3519
Model 3	0	90	Gradient $f(Y)$	0.2047	0.1039	0.7224	0.2066

of where the approximate solution is most different from solutions obtained with each reference model.

Table 2 provides a comparison of the energy norm of the exact error $||\boldsymbol{u}^0 - \boldsymbol{u}||_E$ and the error bound Z. The error metrics presented in Table 2 are normalized by the energy norm of the approximate displacement field, $||\boldsymbol{u}^0||_E$. This normalization quantity does not vary for each reference model. We also define an effectivity index for the error bound as $\eta \doteq \frac{Z}{||\boldsymbol{u}^0 - \boldsymbol{u}||_E}$. An effectivity index of 1 indicates that the error bound matches the true error exactly. Values larger than 1 indicate that the error bound is larger than the true error. Table 3 provides a comparison of the exact errors calculated for other quantities of interest including strain energy, W, the global L_2 norms of the stress and strain fields, and the exact error in the global stretch of the plate Δu_2. We use the Frobenius norm extended to represent the norm of a second-order tensor field $\boldsymbol{\sigma}(x)$ as

$$||\boldsymbol{\sigma}(x)|| \doteq \left(\int_{\Omega} \boldsymbol{\sigma}(x) : \boldsymbol{\sigma}(x) d\Omega \right)^{(1/2)} . \tag{12}$$

From Table 2, it is clear that the global error bound Z provides a rigorous upper bound of $||\boldsymbol{u}^0 - \boldsymbol{u}||_E$ in all cases. The largest total error occurs with respect to Model 1 as the reference model. This occurs because its material orientation of 60° aligns the material direction M_3 consistently closer to the direction of applied loading than the other two reference models. The exact errors calculated directly for other quantities (Table 3) provide additional insight into the errors with respect to each reference model. Generally, the exact error in the L_2 norms of the strain fields are much larger than in the stress fields and the total strain energy. This results from the applied traction boundary conditions and would be expected to reverse for displacement boundary conditions.

The error metrics are also affected by the length scale of large material orientation changes in the reference models. The lowest errors in the strain field norm occur with respect to Model 2, which has layers that alternate material orientation between 45 and 90° at each layer interface. However, the stress field norm and the strain energy have the highest errors with respect to this reference model. This occurs as the stiffer 45° layers dispersed throughout the Model 2 structure constrain deformation in the 90° layers. The result is high local stresses in the 45° layers, but less global strain across the entire structure (see Figures 7 - 8). In Model 3, the material orientations vary from 0° to 90° across the length scale of the entire structure, which results in much more gradual changes in the local stress and strain fields. Thus, the norm of the stress field and the strain energy errors with respect to Model 3 are comparable to those seen with respect to Model 1, which has a uniform material orientation.

The error metrics in Tables 2 - 3 show that the error bound Z identifies the relative severity of errors with respect to the various reference models as long as the length scale of material variations is not too small. However, the global bound alone does not show if the largest differences are in the stress or the strain fields. This motivates extension to goal-orientated error estimation as has been done for random heterogeneous elastic composites [37]. This could be particularly important for AM metals where the length scale of material variations can be small resulting in high local stresses (Model 2).

6.2. Error estimation for variable material orientation angles

We now explore use of the *a posteriori* error estimation framework to provide a range of error bounds based on large sets of reference models. We keep the basic form of Models 1 - 3 and vary the material orientations across a range of arbitrary angles.

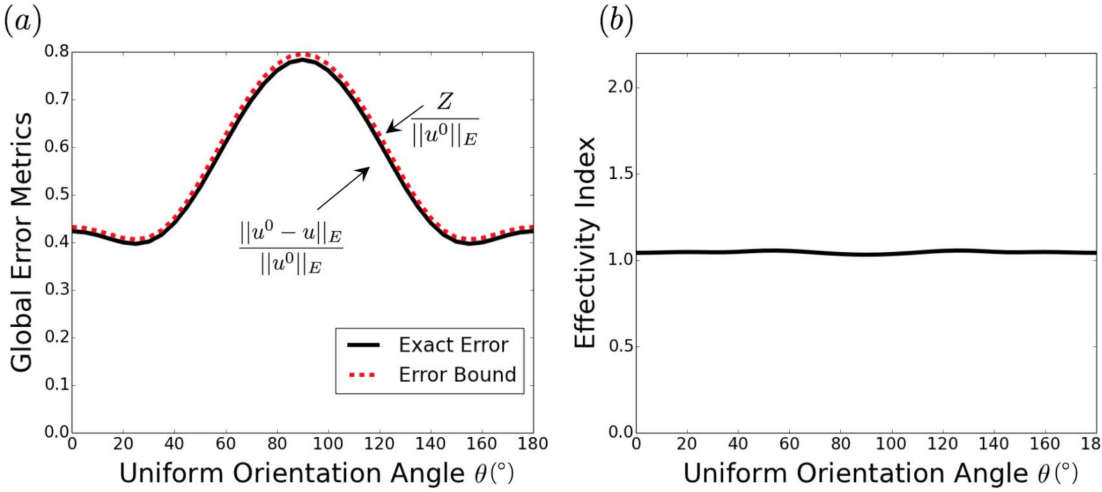

Figure 11. (a) Normalized error bound Z and (b) effectivity index η, for Model 1 with variable orientation angle θ.

Figure 11 shows the normalized error bound, normalized exact total error, and effectivity with respect to reference Model 1 with material orientation angles ranging from $\theta = 0°$ to $\theta = 180°$. A new reference model was generated at intervals of 5° for a total of 36 different models of the Model 1 type. Figure 12 shows the error metrics with

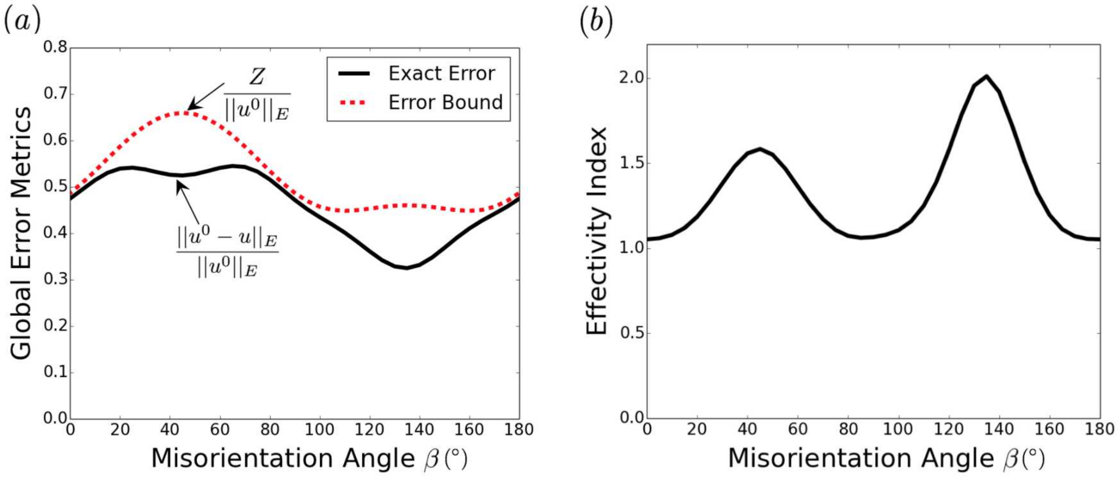

Figure 12. (a) Normalized error bound Z and (b) effectivity index η, for Model 2 with variable misorientation angles β between layers. $\beta = \theta_1 - \theta_2$. In all cases, θ_1 is held fixed at 45°.

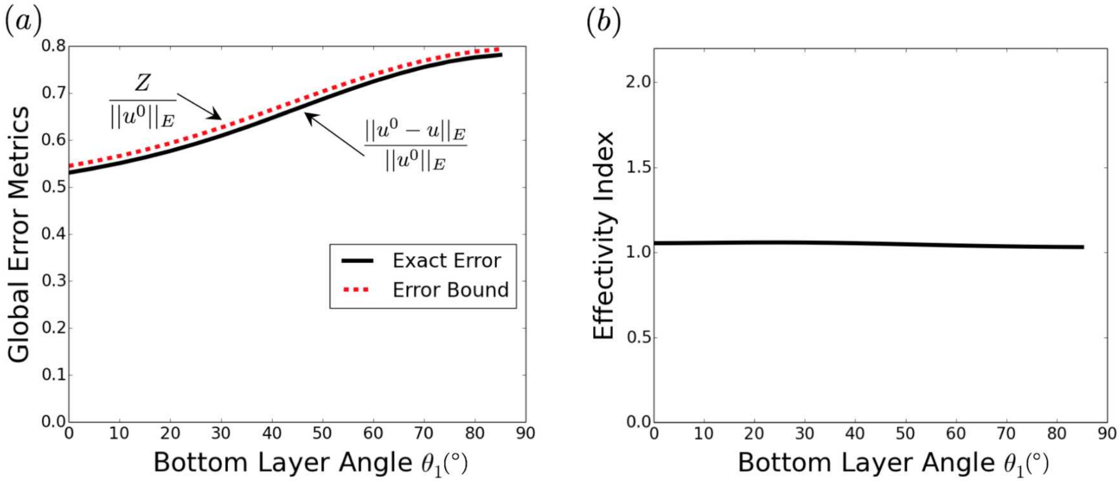

Figure 13. (a) Normalized error bound Z and (b) effectivity index η, for Model 3 with variable bottom layer angle θ_1. The top layer angle is fixed at $\theta_2 = 90°$ such that increasing θ_1 tends toward smaller misorientation between the bottom and the top layers.

respect to Model 2 with various misorientation angles (β) between the alternating layer material orientations. The orientation of M_3 for the first layer is held fixed at $\theta_1 = 45°$, and in the next layer M_3 is rotated counterclockwise by the misorientation angle such that $\theta_2 = \theta_1 + \beta$. This pattern continues throughout the remaining layers which continue to alternate between θ_1 and θ_2. Figure 13 shows error metrics with respect to Model 3 with the orientation of the bottom layer varied between $\theta_1 = 0°$ and $\theta_1 = 90°$. The top layer is held constant at an orientation of $\theta_2 = 90°$. Thus, the global material orientation gradient covers a smaller range of angles from bottom to top as θ_1 increases.

The case of $\theta_1 = 90°$ represents a uniform orientation of all layers at 90°. In all cases, the total error bound and the total exact error are normalized by the energy norm of the approximate displacement field, $||\boldsymbol{u}^0||_E$, which is independent of the reference models. This facilitates comparison of the many reference models and ensures that changes in the error metrics are the only quantities that drive changes in the presented results.

6.2.1. Computational time savings Computing the *a posteriori* error bounds for each reference model was much faster than computing the full reference model solutions. For the study shown in Figure 11, we computed both the error bounds and the exact errors for 36 reference models with different material orientations. Calculating the exact errors required computation of the full finite element solution for each reference model, while the error bound was calculated through the postprocessing approach discussed in Sections 3.1 - 3.2. The error estimation workflow shown in Figure 3 was completed on a single processor and took 2.85 minutes to obtain the approximate model solution followed by 5.4 minutes to compute the error bounds for all 36 reference models. By contrast, it took 2.8 hours to obtain the full finite element solutions for all of the same reference models. This shows that even for elastic analyses, which are considered to be computationally inexpensive, the *a posteriori* error estimation can provide substantial time savings when evaluating many different reference models.

We do note that this time savings is independent of the time required to develop and/or calibrate appropriate reference models. In general, the reference model(s) chosen need not be obtained directly from microstructural information as we have done in this example. Reference model(s) only need to provide a higher fidelity representation of material behavior than the approximate model. For AM metals, however, development of high-fidelity material models is still an active area of research. In some cases, the cost associated with a meso-scale representation of the material microstructure may be necessary for accurate representation of the material behavior. Particularly for such cases, the proposed framework provides a way to quantify model-form errors with respect to microstructure-based models with less computational expense than computing many high-fidelity solutions (such as DNS with embedded microstructures).

6.2.2. Effectiveness of error bounds As seen from Figures 11 - 13 (a), Z provides a strict upper bound of the exact error in the energy norm for all of the reference model variations considered. This promotes confidence that it could be used effectively in an analysis workflow for AM structures as a metric to quickly assess the error in the approximate model result compared to many microstructure-based reference models. Cases with high error bounds could then be further investigated by computing the full solution with these reference models if more details were needed.

Careful design of the reference models and understanding the mechanics of the boundary value problem is still needed to interpret the results of such error estimation sweeps, however. Some knowledge of what features are expected in the microstructure (e.g., macroscale texture vs. local textures vs. no texture) is needed to make sure the reference models are relevant representations of possible material behavior. Additionally, we note that error bounds and associated trends observed over large suites of reference models would vary for different loading conditions, especially since the reference models considered here are not isotropic. For the current example, the maximum error occurs with respect to reference Model 1 with a uniform material orientation of $\theta = 90°$ (Figure 11). For this reference model, the entire structure has the material M_3 direction aligned with the applied load. This material direction has the greatest difference in modulus from the isotropic material model and subsequently results in a large model form error.

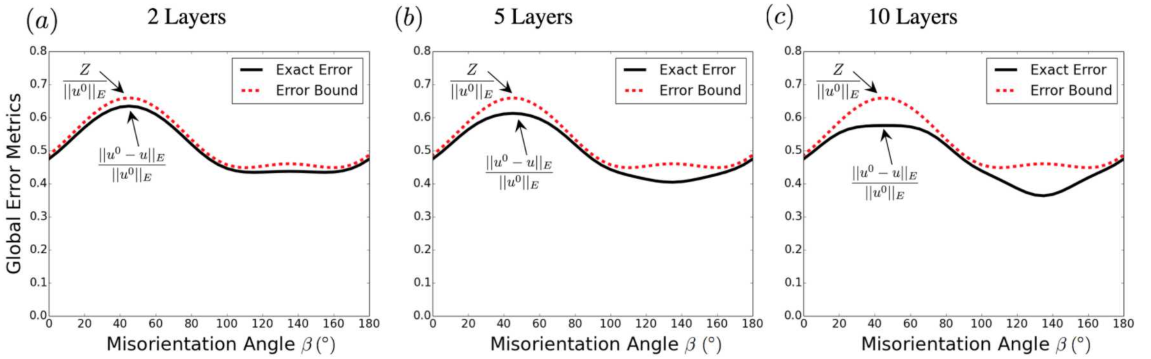

Figure 14. Global error metrics for Model 2 vs. misorientation angle β between layers ($\beta = \theta_1 - \theta_2$) for different number of layers, (a) 2 layers, (b) 5 layers, (c) 10 layers.

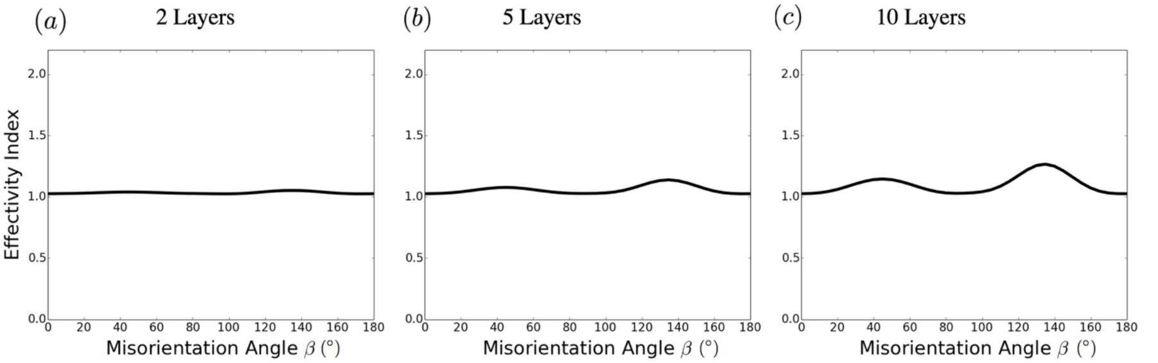

Figure 15. Effectivity of the error bound for Model 2 vs. misorientation angle β between layers ($\beta = \theta_1 - \theta_2$) for different number of layers, (a) 2 layers, (b) 5 layers, (c) 10 layers.

A second feature of the sweeps over many reference models is that while Z always bounds the exact error, this bound is not always tight. This is particularly true for the sweep over misorientation angles between the alternating layers in Model 2. Large discrepancies can be seen between the error indicator and the exact error for misorintation angles between 20 - 80° and between 100 - 160° (Figure 12a), resulting in a high effectivity index up to 2.0 for these particular reference models (Figure 12b). A high effectivity index is generally undesirable, as this metric roughly indicates the percentage by which the true error is overestimated. For the reference models explored here, the only cases where the effectivity index is high are the specific instances mentioned above for Model 2. By contrast, the effectivity index is much closer to 1.0 for both the Model 1 sweep (Figure 11b) and also the Model 3 sweep (Figure 13b). This indicates that the sharp contrast in material properties at the interface between layers in Model 2 is the likely source of this behavior. Model 3 also has different material orientations in each layer, but the misorientation between layers is much more gradual and the corresponding error bound has a much lower effectivity index (Figure 13b).

Figures 14 - 15 present the error metrics for the various misorientation angles with 2, 5 and 10 layers in the Model 2 reference models. Comparing Figures 14 -15 and Figure 12 shows that the error bound becomes less tight as the number of layers increases, and the effectivity index begins to show peaks much greater than 1. This indicates that the sharp gradient in material properties present at the layer interfaces introduces additional complexity in the local stress and strain fields that the single-scale error indicator formulation is unable to capture. If the number of such interfaces is low, the interface effects are small compared with the overall material response and the error bound remains tight. With larger numbers of interfaces, however, the interface effects accumulate and the error bound noticeably deviates from the exact error. Additionally, as more layers are modeled and the individual layers with distinct properties become smaller, the assumption of scale separation between local material variations and areas that can be represented with macroscale properties becomes questionable. This ultimately illustrates the need for multi-scale error estimation techniques, in which the reference models could be DNS of the individual grain responses rather than a set of homogenized macroscale properties. Such multi-scale error estimation techniques have been developed for fiber composite materials (for example, [37]), but have yet to be explored for AM structures. Multi-scale error estimation would be particularly necessary for structures manufactured by powder bed processes, in which the layer thickness is on the order of 30-50 μm and local material variability could occur on a much smaller scale than the reference models studied here.

Lastly, we note that complex part geometries and loading conditions not explored here may also affect the error bound tightness. However, we expect these factors to be secondary drivers compared with the effect of material property interfaces discussed above. The error bound Z is calculated from the approximate solution strain field, the spatial distribution of the approximate stiffness tensor, and the spatial distribution of the reference stiffness tensor (see (9) - (10)). The effects of part geometry and loading would be captured within the approximate model strain fields. Thus, these factors would be incorporated in both the error bound calculation and the reference model solutions. Preliminary studies on more complex part geometries support that reference models with disparate material property interfaces are a stronger contributor to non-tight error bounds.

7. Conclusions

Several methods were explored to model the mechanical response of additively manufactured metal structures with various representations of local and global textures. A 304L stainless steel AM structure with 20 distinct layers was modeled under uniaxial tension loading conditions as an example. *A posteriori* model form error estimation techniques were used to calculate a range of error bounds for a simulation performed with a single approximate material model. The approximate model solution was compared to a set of reference models, with each representing a possible as-built microstructure.

The example presented here considers isotropic, spatially uniform properties as the approximate model and various configurations of material with a pure $\langle 1\,0\,0\rangle$ fiber texture as the reference material. Computational homogenization was used to obtain a higher fidelity representation of AM materials with this textured microstructure. The effective Young's moduli are predicted to be transversely isotropic and differ by a factor of 1.5 between the $\langle 1\,0\,0\rangle$ direction and the other two orthogonal material directions. Over 100 different reference models were generated with the transversely isotropic properties by allowing material orientation to vary throughout the structure. For AM structures where the exact microstructure may be unknown or variable throughout different regions of the structure, this provides a methodology to assess the impact of material variability on the simulation quality.

The *a posteriori* error estimation computations resulted in significant time savings compared to computing the full reference model solutions. Global error bounds on the strain energy norm of the displacement error remained a tight bound on the exact error when the length scale of spatial material changes in the reference models was large. However, material variations over small length scales resulted in pollution errors at layer interfaces, and the global bound noticeably overestimated the exact error. The current findings promote confidence that *a posteriori* model form error estimation could be used effectively in an analysis workflow for AM structures as a metric to quickly obtain quantitative error metrics between an approximate model result and several microstructure-based reference models. For materials with property variation at small length scales, multi-scale error estimation techniques are needed to properly account for the many interfaces present between areas with different properties. Additional development of more accurate reference models for AM structures is also needed in addition to more detailed studies of the assumption of scale separation for these materials.

Acknowledgments

Sandia National Laboratories is a multimission laboratory managed and operated by National Technology and Engineering Solutions of Sandia, LLC, a wholly owned subsidiary of Honeywell International, Inc., for the U.S. Department of Energy's National Nuclear Security Administration under contract DE-NA-0003525. This paper describes objective technical results and analysis. Any subjective views or opinions that might be expressed in the paper do not necessarily represent the views of the U.S. Department of Energy or the United States Government.

References

[1] Francois M, Sun A, King W, Henson N, Tourret D, Bronkhorst C, Carlson N, Newman C, Haut T, Bakosi J, Gibbs J, Livescu V, Vander Wiel S, Clarke A, Schraad M, Blacker T, Lim H, Rodgers T M, Owen S J, Abdeljawad F, Madison J D, Anderson A, Fattebert J L, Ferencz R, Hodge N, Khairallah S and Walton O 2017 *Current Opinion in Solid State and Materials Science* **21** 198–206

[2] Frazier W 2014 *Journal of Materials Engineering and Performance* **23** 1917–1928

[3] Bourell D, Rosen D and Leu M 2014 *3D Printing and Additive Manufacturing* **1** 6–9

[4] Thijs L, Kempen K, Kruth J P and Van Humbeeck J 2013 *Acta Materialia* **61** 1809–1819

[5] Yadollahi A, Shamsaei N, Thompson S M and Seely D W 2015 *Materials Science and Engineering A* **644** 171–183

[6] Wei H, Mazumder J and DebRoy T 2015 *Scientific Reports* **5** 16446

[7] Liu Z and Qi H 2015 *Acta Materialia* **87** 248–258

[8] Niendorf T, Leuders S, Riemer A, Richard H A, Troster T and Schwarze D 2013 *Metallurgical and Materials Transactions B* **44B** 794–796

[9] Dinda G, Dasgupta A and Mazumder J 2012 *Scripta Materialia* **67** 503–506

[10] Suryawanshi J, Prashanth K and Ramamurty U 2017 *Materials Science and Engineering A* **696** 113–121

[11] Yadroitsev I, Krakhmalev P, Yadroitsava I, Johansson S and Smurov I 2013 *Journal of Materials Processing Technology* **213** 606–613

[12] Niendorf T, Brenne F and Schaper M 2014 *Metallurgical and Materials Transactions B* **45B** 1181–1185

[13] Johnson K L, Rodgers T M, Underwood O D, Madison J D, Ford K R, Whetten S R, Dagel D J and Bishop J E 2017 *Computational Mechanics* https://doi.org/10.1007/s00466–017–1516–y

[14] Holesinger T, Carpenter J, Lienert T, Patterson B, Papin P, Swenson H and Cordes N 2016 *JOM* **68** 1000–1011

[15] Riemer A, Leuders S, Thone M, Richard H, Troster T and Niendorf T 2014 *Engineering Fracture Mechanics* **120** 15–25

[16] Saeidi K, Gao X, Zhong Y and Shen Z 2015 *Materials Science and Engineering A* **625** 221–229

[17] Liu J, Xiong W, Behera A, Thompson S and To A C 2017 *International Journal of Solids and Structures* **112** 35–42

[18] Popovich V, Borisov E, Popovich A, Sufiiarov V, Masaylo D and Alzina L 2017 *Materials and Design* **114** 441–449

[19] Dehoff R, Kirka M, Sames W, Bilheux H, Tremsin A, Lowe L and Babu S 2015 *Materials Science and Technology* **31** 931–938

[20] Hu Z and Mahadevan S 2017 *Scripta Materialia* **135** 135–140

[21] Peralta A, Enright M, Megahed M, Gong J, Roybal M and Craig J 2016 *Integrating Materials and Manufacturing Innovation* **5** 1–23

[22] Zohdi T I, Oden J T and Rodin G J 1996 *Computer methods in applied mechanics and engineering* **138** 273–298

[23] Oden J T and Zohdi T I 1997 *Computer methods in applied mechanics and engineering* **148** 367–391

[24] Oden J T and Vemaganti K 1999 *Physica D* **133** 404–415

[25] Brown J A and Bishop J E 2016 *MRS Advances* **1** 2789–2794

[26] Bishop J E and Brown J A 2018 *Computer methods in applied mechanics and engineering*

[27] Glicksman M 2011 *Principles of solidification* (New York: Springer)

[28] Kou S 2003 *Welding metallurgy* 2nd ed (New Jersey: John Wiley and Sons)

[29] Bishop J E, Emery J, Battaile C, Littlewood D and Baines A 2016 *TMS Journal of Materials* **68**

[30] Ainsworth M and Oden J T 2011 *A posteriori error estimation in finite element analysis* (New York: John Wiley and Sons)

[31] Sandia National Laboratories 2012 *CUBIT Geometry and Meshing Toolkit* version 13.2 ed

[32] Team S S M 2016 *Sierra/Solid Mechanics 4.44 User's Guide* Computational Solid Mechanics and Structural Dynamics Department, Engineering Sciences Center, Sandia National Laboratories Albuquerque, NM 87185 4th ed

[33] Ledbetter H 1984 *Physica Status Solidi A* **85** 89–96

[34] Bishop J E, Emery J, Field R, Weinberger C and Littlewood D 2015 *Computer methods in applied mechanics and engineering* **287** 262–289

[35] Matous K, Geers M, Kouznetsova V and Gillman A 2017 *Journal of Computational Physics* **330** 192–220

[36] Hitzler L, Hirsch J, Heine B, Merkel M, Hall W and Ochsner A 2017 *Materials* **10** 1136

[37] Romkes A, Oden J T and Vemaganti K 2006 *Mechanics of Materials* **38** 859–872